Dalton Transactions

ROYAL SOCIETY OF CHEMISTRY

PAPER

View Article Online
View Journal | View Issue

Cite this: *Dalton Trans.*, 2023, **52**, 14928

Iron(II) complexes of 2,6-bis(imidazo[1,2-*a*]pyridin-2-yl)pyridine and related ligands with annelated distal heterocyclic donors†

Rafal Kulmaczewski and Malcolm A. Halcrow *

Received 23rd August 2023,
Accepted 30th September 2023

DOI: 10.1039/d3dt02747c

rsc.li/dalton

Following a published synthesis of 2,6-bis(imidazo[1,2-*a*]pyridin-2-yl)pyridine (L^1), treatment of α,α′-dibromo-2,6-diacetylpyridine with 2 equiv. 2-aminopyrimidine or 2-aminoquinoline in refluxing acetonitrile respectively gives 2,6-bis(imidazo[1,2-*a*]pyrimidin-2-yl)pyridine (L^2) and 2,6-bis(imidazo[1,2-*a*]quinolin-2-yl)pyridine (L^3). Solvated crystals of $[Fe(L^1)_2][BF_4]_2$ (**1[BF$_4$]$_2$**) and $[Fe(L^2)_2][BF_4]_2$ (**2[BF$_4$]$_2$**) are mostly high-spin, although one solvate of **1[BF$_4$]$_2$** undergoes thermal spin-crossover on cooling. The iron coordination geometry is consistently distorted in crystals of **2[BF$_4$]$_2$** which may reflect the influence of intramolecular, inter-ligand N···π interactions on the molecular conformation. Only 1 : 1 Fe : L^3 complexes were observed in solution, or isolated in the solid state; a crystal structure of $[FeBr(py)_2L^3]Br{\cdot}0.5H_2O$ (py = pyridine) is presented. A solvate crystal structure of high-spin $[Fe(L^4)_2][BF_4]_2$ (L^4 = 2,6-di{quinolin-2-yl}pyridine; **4[BF$_4$]$_2$**) is also described, which exhibits a highly distorted six-coordinate geometry with a helical ligand conformation. The iron(II) complexes are high-spin in solution at room temperature, but **1[BF$_4$]$_2$** and **2[BF$_4$]$_2$** undergo thermal spin-crossover equilibria on cooling. All the compounds exhibit a ligand-based emission in solution at room temperature. Gas phase DFT calculations mostly reproduce the spin state properties of the complexes, but show small anomalies attributed to intramolecular, inter-ligand dispersion interactions in the sterically crowded molecules.

Introduction

Spin-crossover (SCO) complexes continue to be heavily studied.[1–5] Controlling spin state properties is vital for the design of new catalysts[6–10] or photosensitisers[11,12] from base metal centres.[13] Moreover, solid SCO materials are useful testbeds for the crystal engineering of phase transitions in molecular crystals,[14,15] while time-resolved spectroscopic and diffraction methods are shedding new light on the atomistic mechanisms of SCO-induced phase transitions.[16–18] SCO switching in thin films,[19,20] nanoparticles,[21,22] monolayers and single molecules[19,23–25] is well-established, leading to the use of SCO complexes in nanomolecular electronics.[26,27] Lastly, SCO molecules are useful switching components in functional materials which exploit their thermochromism,[28,29] or other materials properties associated with the spin transition.[30–35] Alternatively, SCO auxiliaries can control fluorescence,[36,37] conductivity,[38] magnetic[39–41] or ferroelectric[42] properties in multifunctional composite crystals or soft materials.[43]

Iron(II) complexes of tridentate tris-heterocyclic ligands are particularly fruitful for SCO chemistry.[44,45] Iron(II) complexes of ligands derived from trispyrazolylborate,[46] trispyrazolylmethane,[46,47] 2,6-di(1*H*-benzimidazol-2-yl)pyridine (bimpy)[48] and regioisomers of 2,6-di(pyrazolyl)pyridine (bpp)[49–52] can all exhibit SCO at accessible temperatures. These ligand classes can be functionalised using appropriate synthetic starting materials or through functional group manipulations, giving steric and electronic control over the spin states of their iron complexes.[48,49,52–56] It also allows functional substituents, long alkyl chains or tether groups to be appended to SCO complexes, producing multifunctional materials or nanostructures based on SCO switches. Complexes of the bimpy[57,58] and bpp[59–64] ligand families have been particularly useful for the latter goal.

Notwithstanding its multifunctional derivatives, $[Fe(bimpy)_2]^{2+}$ was an early example of a fluorescent SCO complex,[65] which have been increasingly developed during the last ten years.[36,37] With that in mind, we investigated

School of Chemistry, University of Leeds, Woodhouse Lane, Leeds, UK LS2 9JT. E-mail: m.a.halcrow@leeds.ac.uk

†Electronic supplementary information (ESI) available: Synthetic protocols and characterisation data for the ligands in this work; experimental data, refinement details, figures and tables for the crystal structure determinations; additional solid and solution phase characterisation data; and details of the minimised structures from the DFT calculations. CCDC 2288873–2288881. For ESI and crystallographic data in CIF or other electronic format see DOI: https://doi.org/10.1039/d3dt02747c

$[Fe(1\text{-bip})_2]^{2+}$ (1-bip = 2,6-bis{indazol-1-yl}pyridine) and $[Fe(2\text{-bip})_2]^{2+}$ (2-bip = 2,6-bis{indazol-2-yl}pyridine), with the latter being an isosteric analogue of the bimpy complex.[66] These also exhibit a ligand-based fluorescence in solution at room temperature, but whose wavelength was unaffected by the spin state of the complexes.[66,67]

Ruthenium complexes of 2,6-bis(imidazo-[1,2-*a*]pyridin-2-yl)pyridine (L^1; Scheme 1) and its derivatives have been studied by Song *et al.*, as catalysts for a number of reactions.[68–72] Following our study of bip ligands, which are constitutional isomers of L^1, we now report the iron(II) complex chemistry of L^1 and two new analogues, 2,6-bis(imidazo-[1,2-*a*]pyrimidin-2-yl)pyridine (L^2) and 2,6-bis(imidazo-[1,2-*a*]quinolin-2-yl)pyridine (L^3; Scheme 1). We also include a re-investigation of previously reported $[Fe(L^4)_2]^{2+}$ (L^4 = 2,6-di{quinol-2-yl}pyridine, dqp).[73]

Results and discussion

Reaction of 2,6-diacetylpyridine with *N*-bromosuccinimide in refluxing acetonitrile affords α,α′-dibromo-2,6-diacetylpyridine, in moderate yield. Treatment of that intermediate with 2 equiv. 2-aminopyridine in refluxing acetonitrile gives L^1 (Scheme 1), in *ca.* 60% yield after purification.[68] The latter reaction is sensitive to the purity of the α,α′-dibromo-2,6-diacetylpyridine starting material, which should be synthesised *in situ* and used immediately for the best results. We also screened other 2-aminoazine reagents in this protocol, which afforded L^2 (from 2-aminopyrimidine) and L^3 (from 2-aminoquinoline) in NMR purity. An attempted synthesis of 2,6-bis(imidazo[1,2-*a*]pyrazinyl)pyridine from aminopyrazine by this method gave a product that was too insoluble to characterise, however (ESI†). Ligand L^4 was synthesised for this study by a literature procedure.[73,74]

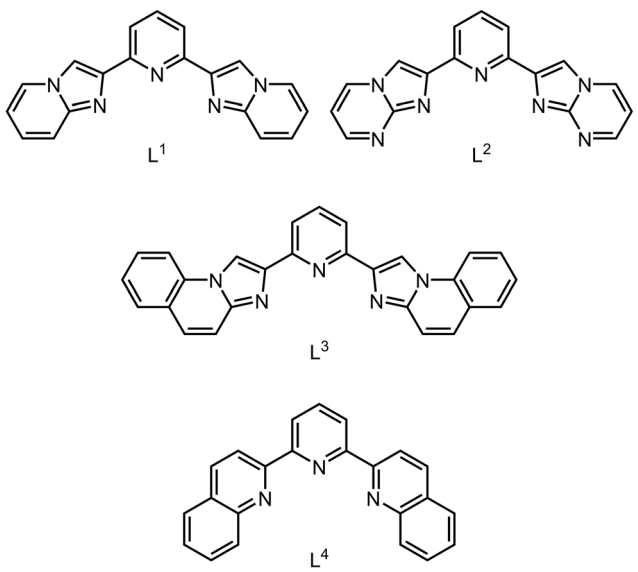

Scheme 1 The ligands investigated in this study.

Treatment of $Fe[BF_4]_2{\cdot}6H_2O$ with 2 equiv. L^1 or L^2 in acetonitrile affords $[Fe(L^1)_2][BF_4]_2$ (**1[BF$_4$]$_2$**) and $[Fe(L^2)_2][BF_4]_2$ (**2[BF$_4$]$_2$**) as brown polycrystalline solids after the usual work up. Both complexes form solvated single crystals and, while **2[BF$_4$]$_2$** was obtained as a solvent-free material after drying *in vacuo*, samples of **1[BF$_4$]$_2$** always contained residual solvent or lattice water by microanalysis. Since the spin state properties of some solvated iron complexes depend significantly on the lattice solvent,[75–81] multiple solvates of **1[BF$_4$]$_2$** and **2[BF$_4$]$_2$** were isolated for characterisation.

Four crystalline solvates of **1[BF$_4$]$_2$** were characterised by X-ray diffraction, three of which can be considered together. The asymmetric unit of **1[BF$_4$]$_2$**·MeCN and **1[BF$_4$]$_2$**·*m*$MeNO_2$ ($m \approx 0.8$; both orthorhombic, space group *Pccn*, $Z = 4$) contains half a formula unit. Their iron atom lies on a crystallographic C_2 axis, so the complex molecule has perfect C_2 symmetry (Fig. 1). The solvate **1[BF$_4$]$_2$**·1.5MeOH (orthorhombic, $Pna2_1$, $Z = 4$) has similar unit cell dimensions and crystal packing as the first two solvates, but lacks their crystallographic inversion symmetry. All three solvates contain high-spin complex mole-

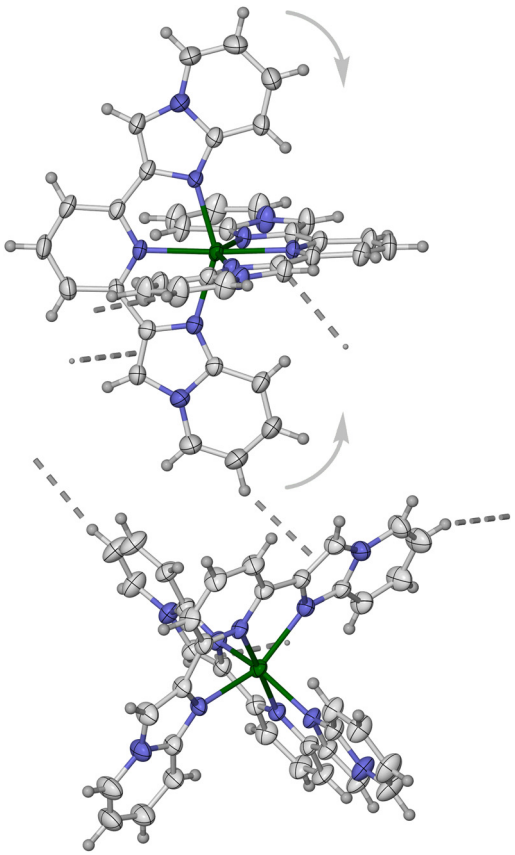

Fig. 1 Two $[Fe(L^1)_2]^{2+}$ molecules in **1[BF$_4$]$_2$**·MeCN, related by $1 - x$, $\frac{1}{2} + y$, $\frac{1}{2} - z$. The intermolecular C–H···π contact that may inhibit thermal SCO in the three near-isomorphous solvates of **1[BF$_4$]$_2$** is shown in grey, which is positioned to inhibit displacement of those imidazopyridyl groups in the direction shown which would accompany SCO. A space-filling view of this interaction is in Fig. S10.† Colour code: C, white; H, pale grey; Fe, green; N, blue.

cules at 120 K, with near-regular coordination geometries showing minor deviations from idealised D_{2d} symmetry (Table 1). The cations associate into zig-zag chains through strong face-to-face π···π interactions, involving one imidazopyridyl arm of each ligand. The chains alternate down the *c* axis, along the [1$\bar{1}$0] and [$\bar{1}$10] crystal vectors in the *Pccn* solvates (the unit cell axes are exchanged in the *Pna*2$_1$ setting).

As discussed below, there is nothing in the molecular geometry of these three solvates that should prevent thermal SCO on cooling. Rather, we attribute their high-spin nature to an intermolecular C–H···π contact between molecules in neighbouring cation chains (Fig. 1). While the interaction is not notably short, it is positioned to inhibit the displacement of two of the imidazo-[1,2-*a*]pyridin-2-yl groups that would accompany contraction of those Fe–N bonds during SCO.

While samples of **1[BF$_4$]$_2$**·MeCN and **1[BF$_4$]$_2$**·1.5MeOH were homogeneous, red needles of **1[BF$_4$]$_2$**·*m*MeNO$_2$ were often mixed with small black prisms which had the crystallographic composition **1[BF$_4$]$_{1.6}$[SiF$_6$]$_{0.2}$**·1.7MeNO$_2$·0.3Et$_2$O (triclinic, *P*$\bar{1}$, *Z* = 2). The fractional SiF_6^{2-} content of these crystals should arise from reaction of the silica crystallisation vials with adventitious F^-, produced by hydrolysis of BF_4^- during the crystallisation process.[86] The complex in this crystal is low-spin at 120 K from its metric parameters, which confirms the low-spin state of **1[BF$_4$]$_2$** is thermodynamically accessible (Table 1).

1[BF$_4$]$_{1.6}$[SiF$_6$]$_{0.2}$·1.7MeNO$_2$·0.3Et$_2$O differs from the other solvates of that complex, in adopting a 'terpyridine embrace' packing motif.[87] The complex cations interdigitate into four-fold layers in the ($\bar{1}$10) crystal plane, through edge-to-face and face-to-face π···π interactions involving all their imidazopyridyl residues. Nearest neighbour molecules within the layers are related by crystallographic inversion centres, while the layers propagate in 3D by translation along *a* and *b*. While they are not perfectly isomorphous, the crystal packing in **1[BF$_4$]$_{1.6}$[SiF$_6$]$_{0.2}$**·1.7MeNO$_2$·0.3Et$_2$O resembles its regioisomer [Fe(2-bip)$_2$][BF$_4$]$_2$·2MeNO$_2$, which adopts a closely related terpyridine embrace packing motif.[66]

The solvates of **1[BF$_4$]$_2$** retain crystallinity by powder diffraction upon exposure to air (Fig. S15†). Magnetic susceptibility data show **1[BF$_4$]$_2$**·MeCN and **1[BF$_4$]$_2$**·1.5MeOH are both high-spin between 5–300 K, which is consistent with their crystal structures at 120 K. Another sample crystallised in small quantities from acetone/diethyl ether was also high-spin (Fig. S16†). The small crystal size of the MeNO$_2$ solvates made it impossible to separate them manually for magnetic characterisation. However, a mixed-phase sample was high-spin at room temperature with an abrupt, partial spin-transition at $T_{\frac{1}{2}}$ = 178 K occurring in *ca.* 45% of the material. That is consistent with a mixture of high-spin and SCO-active phases, as observed crystallographically. Iron(II) complexes related to **1[BF$_4$]$_{1.6}$[SiF$_6$]$_{0.2}$**·1.7MeNO$_2$·0.3Et$_2$O with terpyridine embrace lattices often show similarly abrupt thermal spin-transitions.[66,88,89]

Three solvates of **2[BF$_4$]$_2$** were also crystallised: isomorphous **2[BF$_4$]$_2$**·1.5MeCN and **2[BF$_4$]$_2$**·Me$_2$CO (both triclinic, *P*$\bar{1}$, *Z* = 2) and **2[BF$_4$]$_2$**·3.5MeNO$_2$·0.5Et$_2$O (also triclinic, *P*$\bar{1}$, *Z* = 2 but not isomorphous with the other solvates). These are all

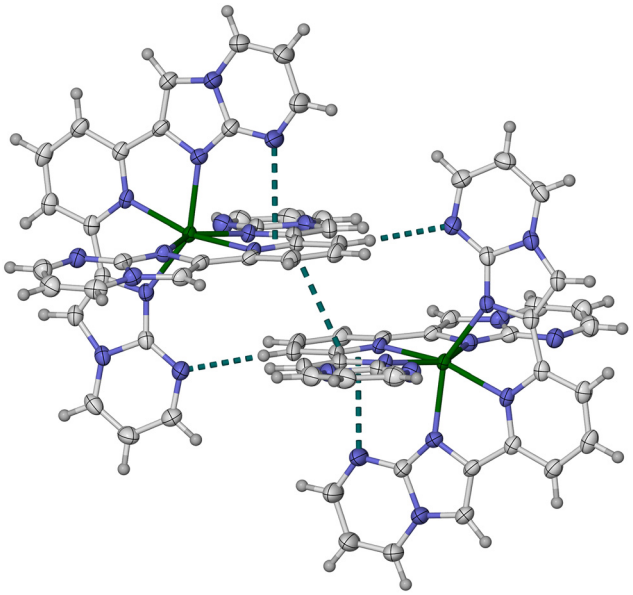

Fig. 2 A centrosymmetric pair of $[Fe(L^2)_2]^{2+}$ molecules in **2[BF$_4$]$_2$**·1.5MeCN, showing the intramolecular n···π, intermolecular π···π and intermolecular C–H···N contacts involving the L^2 ligands. Colour code: C, white; H, pale grey; Fe, green; N, blue.

Table 1 Selected bond lengths and angular parameters for the solvate crystals of **1[BF$_4$]$_2$** at 120 K (Å, °, Å^3). A full list of bond lengths and angles is in Table S2 (ESI†)[a]

	1[BF$_4$]$_2$·MeCN[b]	**1[BF$_4$]$_2$**·*m*MeNO$_2$[b]	**1[BF$_4$]$_{1.6}$[SiF$_6$]$_{0.2}$**·1.7MeNO$_2$·0.3Et$_2$O	**1[BF$_4$]$_2$**·MeOH
Fe–N{pyridyl}	2.175(3)	2.168(3)	1.920(3), 1.924(3)	2.171(4), 2.171(4)
Fe–N{imidazopyridyl}	2.191(3), 2.199(4)	2.195(3), 2.199(3)	1.979(3)–2.002(3)	2.193(4)–2.201(4)
V_{Oh}	12.901(15)	12.873(11)	9.896(8)	12.908(15)
Σ	144.4(5)	145.2(4)	81.5(4)	143.5(5)
Θ	473	476	268	470
ϕ	176.42(18)	175.81(14)	178.78(11)	175.96(14)
θ	89.66(3)	89.87(2)	88.89(2)	89.93(3)

[a] V_{Oh}, Σ and Θ are indices showing the spin state of the complex,[82,83] while ϕ and θ measure the orientations of the two tridentate ligands in the molecule.[84,85] Typical values for these parameters in complexes related to **1[BF$_4$]$_2$** are given in ref. 51 and 52. [b] The complex cations in these crystals have crystallographic C_2 symmetry.

crystallographically high-spin at 120 K. However, in contrast to **1[BF$_4$]$_2$**, the complex coordination geometry in the **2[BF$_4$]$_2$** solvates is significantly distorted from its idealised D_{2d} symmetry (Fig. 2). This is particularly reflected in the *trans*-N{pyridyl}–Fe–N{pyridyl} angle (ϕ, Table 2) which lies between 156.26(12)–164.72(7)°, significantly lower than its ideal value of 180°. This type of distortion is well-known in high-spin [Fe(bpp)$_2$]$^{2+}$ derivatives, and reflects an angular Jahn–Teller distortion of the complex along the O_h–D_{3d} coordinate.[51,52] The distortion has a shallow energy profile,[85,89,90] and [Fe(bpp)$_2$]$^{2+}$ derivatives with 148 ≤ ϕ ≤ 180° have been reported.[91,92]

Since the distortion is a property of the high-spin state, SCO in a distorted complex requires a significant structural rearrangement to the more regular coordination geometry preferred by the low-spin form. Hence, SCO becomes more disfavoured as ϕ (and θ, Table 2) deviate increasingly from their ideal values in crystalline complexes.[85,90] The distortions in **2[BF$_4$]$_2$** lie in the range where SCO is rarely observed (Fig. 3).[91,92] Consistent with that, all the solvates of **2[BF$_4$]$_2$** remain high-spin between 5–300 K from magnetic susceptibility data (Fig. S25†).

These distorted coordination geometries facilitate two different supramolecular interactions involving the L^2 ligands (Fig. 2). First, are intramolecular n···π contacts between the imidazopyrimidinyl *N*8 atom of one ligand, and a pyridyl C–N bond of the other ligand.[93] Second, is intermolecular π···π overlap between nearest neighbour molecules in the lattice. This is always accompanied by a weak intermolecular C–H···N contact to the other imidazopyrimidinyl *N*8 atom acceptor, from the same ligand that forms the intramolecular n···π interaction. One ligand in each molecule in isomorphous **2[BF$_4$]$_2$**·1.5MeCN and **2[BF$_4$]$_2$**·MeCO takes part in these interactions, associating the cations into centrosymmetric pairs. In contrast, both ligands in each molecule of **2[BF$_4$]$_2$**·3.5MeNO$_2$·0.5Et$_2$O form the same set of pairwise interactions, affording zig-zag chains of strongly linked cations (Fig. S20 and S21†). The larger ϕ distortion in this solvate facilitates close approach of the neighbour molecule forming its second intramolecular n···π interaction.

Samples of **2[BF$_4$]$_2$**·1.5MeCN and **2[BF$_4$]$_2$**·Me$_2$CO retain crystallinity on exposure to air, but **2[BF$_4$]$_2$**·3.5MeNO$_2$·0.5Et$_2$O decomposes through solvent loss to a poorly crystalline red powder. All these materials are high-spin above 5 K, as expected from their crystallographic coordination geometries (Fig. 3).

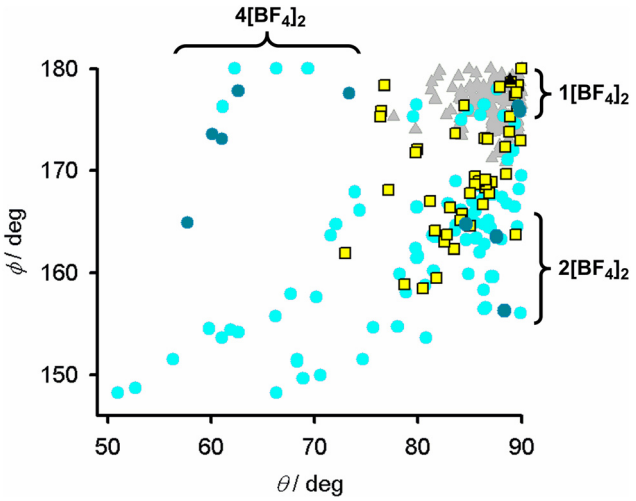

Fig. 3 Distortion parameters for [Fe(1-bpp)$_2$]$^{2+}$ (1-bpp = 2,6-di{pyrazol-1-yl}pyridine) derivatives which are low-spin (grey triangles); high-spin and SCO-active (yellow squares); or remain high-spin on cooling (cyan circles).[84,85] Compounds in this work are plotted with the same symbols in darker colouration. The graph is adapted from ref. 92.

In contrast to L^1 and L^2, treatment of Fe[BF$_4$]$_2$·6H$_2$O with 2 equiv. L^3 yields brown solids whose microanalyses are consistent with the formulae [FeL^3][BF$_4$]$_2$·*y*(solvent); that is, with a 1 : 1 Fe : L^3 stoichiometry. Consistent with that, freshly prepared solutions of a 1 : 2 molar mixture of Fe[BF$_4$]$_2$·6H$_2$O and L^3 contain a significant amount of uncoordinated ligand by NMR, which is not observed in solutions of **1[BF$_4$]$_2$** and **2[BF$_4$]$_2$**. Single crystals were ultimately obtained from a sample of formula [FeBr(py)$_2$L^3]Br·0.5H$_2$O (py = pyridine; Fig. 4). The tridentate L^3 ligand in that complex displays no obvious steric hindrance to explain its reluctance to form a homoleptic iron complex. Other physical characterisation was performed on a sample with the analytical formula [FeL^3][BF$_4$]$_2$·H$_2$O, labelled **3′[BF$_4$]$_2$**·H$_2$O.

Lastly, in 1969 Sinn *et al.* reported that [Fe(L^4)$_2$][ClO$_4$]$_2$ (**4[ClO$_4$]$_2$**) is high-spin above 85 K in the solid state.[73] We have re-investigated this complex as its BF$_4^-$ salt, **4[BF$_4$]$_2$**. Single crystals of **4[BF$_4$]$_2$**·1.39MeCN·0.125Et$_2$O·0.25H$_2$O (monoclinic, $P2_1/c$, Z = 16, *i.e.* Z' = 4) contain four crystallographically unique complex molecules in their asymmetric unit. The four molecules are distinguishable by their molecular conformations, which are strongly flattened with a helical twist

Table 2 Selected bond lengths and angular parameters for the solvate crystals of **2[BF$_4$]$_2$** at 120 K (Å, °, Å^3). A full list of bond lengths and angles is in Table S4 (ESI†). See Table 1 and the ESI† for definitions of the structural indices[82–85]

	2[BF$_4$]$_2$·1.5MeCN	**2[BF$_4$]$_2$**·Me$_2$CO	**2[BF$_4$]$_2$**·3.5MeNO$_2$·0.5Et$_2$O
Fe–N{pyridyl}	2.148(2), 2.154(2)	2.1499(16), 2.1538(16)	2.160(3), 2.162(3)
Fe–N{imidazopyrimidyl}	2.183(2)–2.201(2)	2.1849(18)–2.2076(17)	2.196(3)–2.212(3)
V_{Oh}	12.536(10)	12.586(6)	12.430(12)
Σ	140.3(3)	140.4(2)	144.8(4)
Θ	467	463	482
ϕ	163.52(9)	164.72(7)	156.26(12)
θ	87.59(3)	84.65(1)	88.37(2)

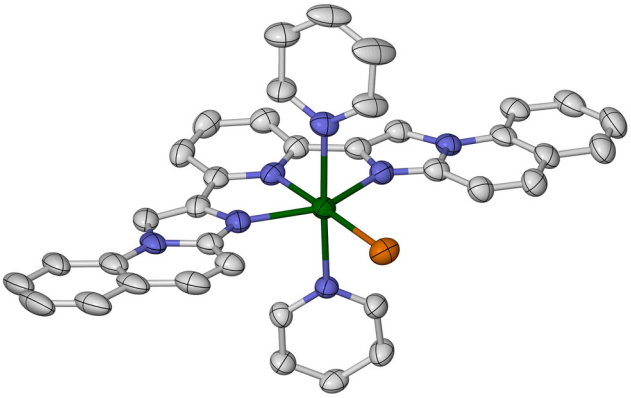

Fig. 4 The complex cation in $[FeBr(py)_2L^3]Br{\cdot}0.5H_2O$. Displacement ellipsoids are at the 50% probability level, and H atoms are omitted for clarity. Colour code: C, white; Br, orange; Fe, green; N, blue.

Table 3 Selected bond lengths and angular parameters for the four unique cation environments in crystals of 4$[BF_4]_2{\cdot}1.39MeCN{\cdot}0.125Et_2O{\cdot}0.25H_2O$ at 120 K (Å, °, Å^3). A full list of bond lengths and angles is in Table S7 (ESI†). See Table 1 and the ESI† for definitions of the structural indices[82–85]

	Molecule A	Molecule B[a]	Molecule C	Molecule D
Fe–N {pyridyl}	2.073(6), 2.102(6)	2.100(5), 2.148(9)/ 2.049(15)	2.088(5), 2.088(5)	2.114(5), 2.099(4)
Fe–N {quinolinyl}	2.221(5)–2.319(6)	2.235(10)–2.335(8)	2.252(5)–2.298(6)	2.249(5)–2.286(5)
V_{Oh}	12.73(2)	12.85(3)/ 12.99(4)	12.94(2)	13.149(18)
Σ	174.6(7)	195.5(11)/ 172.9(13)	177.3(7)	153.6(7)
Θ	486	529/482	476	476
ϕ	164.9(2)	173.6(3)/ 173.1(5)	177.8(2)	177.6(2)
θ	57.75(5)	60.15(7)/ 61.04(9)	62.64(5)	73.38(4)

[a] Ligand N(28B)–C(53B) is disordered over two sites, with refined occupancies of 0.61 : 0.39. Values involving both ligand disorder sites are given in the table.

(Fig. 5). This is manifested by the dihedral angle between the least squares planes of the L^4 ligands in each molecule (θ, Table 3 and Fig. 3).[84] Molecules A–D exhibit $57.75(5) \leq \theta \leq 73.38(4)$ which is strongly reduced from the idealised value of 90°, while molecule A also has a significant ϕ distortion. The resultant helical ligand conformations give each metal centre a Λ or Δ chirality; the centrosymmetric crystal lattice contains equal numbers of Λ- and Δ-helical molecules. Space-filling models imply the helical distortion is induced by steric repulsion between the quinolyl *C*8–H groups on each ligand,[93] and the pyridyl ring of the other ligand in the molecule. One other homoleptic complex of L^4 has also been crystallographically characterised, namely a solvate of $[Co(L^4)_2][PF_6]_2$. That complex has a much smaller helical conformational distortion, with $\phi = 180$ and $\theta = 79.5–80.9°$.[94]

The $[Fe(L^4)_2]^{2+}$ cations associate into homochiral helical columns in the crystal lattice, through weak intermolecular π···π interactions between their quinolyl groups. The molecules stack as ···A···B···D···C··· down the $[10\bar{1}]$ crystal vector (Fig. S33–S35†), and left and right-handed columns are arranged into strips whose helicity alternates along *c*.

As discussed above, the twisted coordination geometries in $\mathbf{4[BF_4]_2}$ should strongly favour its high-spin state and inhibit SCO. Consistent with that, the solid complex is fully high-spin between 5–300 K (Fig. S36†).

Solutions of $\mathbf{1[BF_4]_2}$, $\mathbf{2[BF_4]_2}$ and $\mathbf{4[BF_4]_2}$ are paramagnetic, with just one C_2 or *m*-symmetric ligand environment by ^{1}H NMR (Fig. S37–S39†). The NMR spectrum of $\mathbf{4[BF_4]_2}$ in CD_3CN also contains *ca.* 0.1-equiv of uncoordinated L^4, implying a minor degree of ligand dissociation in solution for that complex. No free ligand was detected in solutions of $\mathbf{1[BF_4]_2}$ and $\mathbf{2[BF_4]_2}$, however.

The spin states of the complexes were monitored by variable temperature Evans method measurements (Fig. 6). Each compound is fully, or predominantly, high-spin at 300 K which is consistent with their paramagnetic NMR spectra. Solutions of $\mathbf{1[BF_4]_2}$ and $\mathbf{2[BF_4]_2}$ clearly show the onset of SCO equilibria on cooling, which were fitted to the following parameters: for $\mathbf{1[BF_4]_2}$, $T_{\frac{1}{2}} = 237 \pm 3$ K, $\Delta H = 19.3 \pm 1.3$ kJ mol^{-1}, $\Delta S = 81 \pm 6$ J mol^{-1} K^{-1}; for $\mathbf{2[BF_4]_2}$, $T_{\frac{1}{2}} = 251 \pm 1$ K, $\Delta H = 22.4 \pm 0.7$ kJ mol^{-1}, $\Delta S = 89 \pm 3$ J mol^{-1} K^{-1}. The fitted thermodynamic data are typical for iron(II) complexes of N-donor

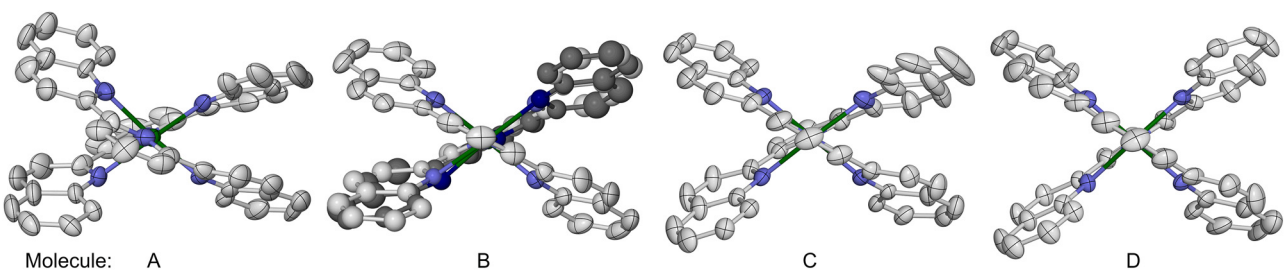

Fig. 5 The four unique $[Fe(L^4)_2]^{2+}$ molecules in $4[BF_4]_2{\cdot}1.39MeCN{\cdot}0.125Et_2O{\cdot}0.25H_2O$, viewed along their N{pyridyl}–Fe–N{pyridyl} vectors. Both ligand disorder sites in molecule B are included and distinguished with pale and dark colouration. The crystallographic views of molecules C and D have been inverted, to give them the same handedness as molecules A and B. Displacement ellipsoids are at the 50% probability level, and H atoms are omitted for clarity. Colour code: C, white or dark grey; H, pale grey; Fe, green; N, pale or dark blue.

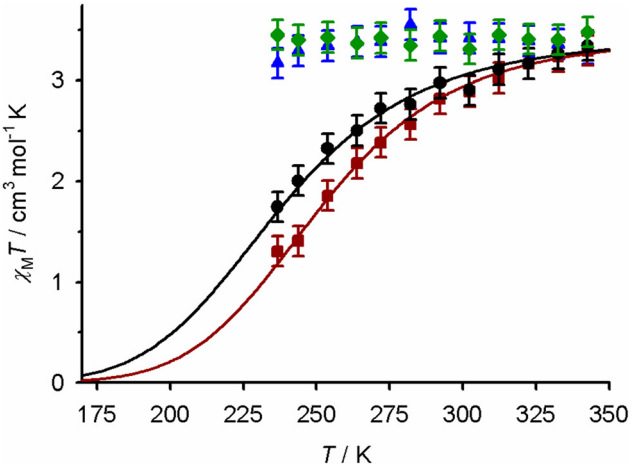

Fig. 6 Magnetic susceptibility data in CD_3CN solution for: **1[BF$_4$]$_2$** (black ●), **2[BF$_4$]$_2$** (red ■), **3′[BF$_4$]$_2$·H$_2$O** (blue ▲), and **4[BF$_4$]$_2$** (green ◆). The lines show the best fit of the data for **1[BF$_4$]$_2$** and **2[BF$_4$]$_2$** to a thermodynamic SCO equilibrium (eqn (1) and (2), Experimental section).

ligands,[55,95,96] with no apparent contributions from other solution equilibria.[97,98] In contrast, **3′[BF$_4$]$_2$·H$_2$O** and **4[BF$_4$]$_2$** remain high-spin over the liquid range of the solvent.

Ligands L^1–L^4 have a blue fluorescence in acetonitrile solution at room temperature (Fig. 7). Comparison with analogous model compounds implies the near-UV absorptions and emission maxima for L^1–L^3 should be centred on their imidazo[1,2-*a*]azine residues.[99–101] The L^2 emission [λ^{em}_{max} = 457 nm] lies at longer wavelength than for L^1 [423 nm], L^3 [434 nm] and L^4 [435 nm], which might reflect additional dipolar interactions between L^2 and the solvent *via* its imidazopyrimidinyl *N*8 atoms.[93,102] Measurements in different solvents to probe that suggestion were hampered by the poor solubility of L^2, however. The absorption and emission spectra for L^4 in Fig. 7 are consistent with literature data.[94,103,104]

The complexes have a weak blue emission under the same conditions, at 445 ≤ λ^{em}_{max} ≤ 453 nm for **1[BF$_4$]$_2$**–**3′[BF$_4$]$_2$**, and λ^{em}_{max} = 499 nm for **4[BF$_4$]$_2$** (Fig. 7). In most cases, these emissions are red-shifted compared to the corresponding free ligand. The exception is **2[BF$_4$]$_2$**, whose emission maximum [445 nm] is essentially identical to **1[BF$_4$]$_2$** [446 nm], but is slightly blue-shifted compared to L^2. That supports the involvement of solvation interactions in the longer wavelength emission of L^2 (see above). Those interactions would be quenched in **2[BF$_4$]$_2$** whose imidazopyrimidinyl *N*8 lone pairs[93] are oriented towards the interior of the complex (Fig. 2).

Gas phase DFT calculations were performed to confirm the spin state properties of the complexes, using the B86PW91 functional and def2-SVP basis set. Similar protocols performed well in benchmark studies comparing the spin states in different iron(II) complexes,[105–107] and we have used this method to elucidate structure:function relationships for SCO in several iron(II) complex families with heterocyclic ligands.[108–112] The hypothetical homoleptic complex [Fe(L^3)$_2$]$^{2+}$ (**3^{2+}**) was included in the calculations, for comparison with

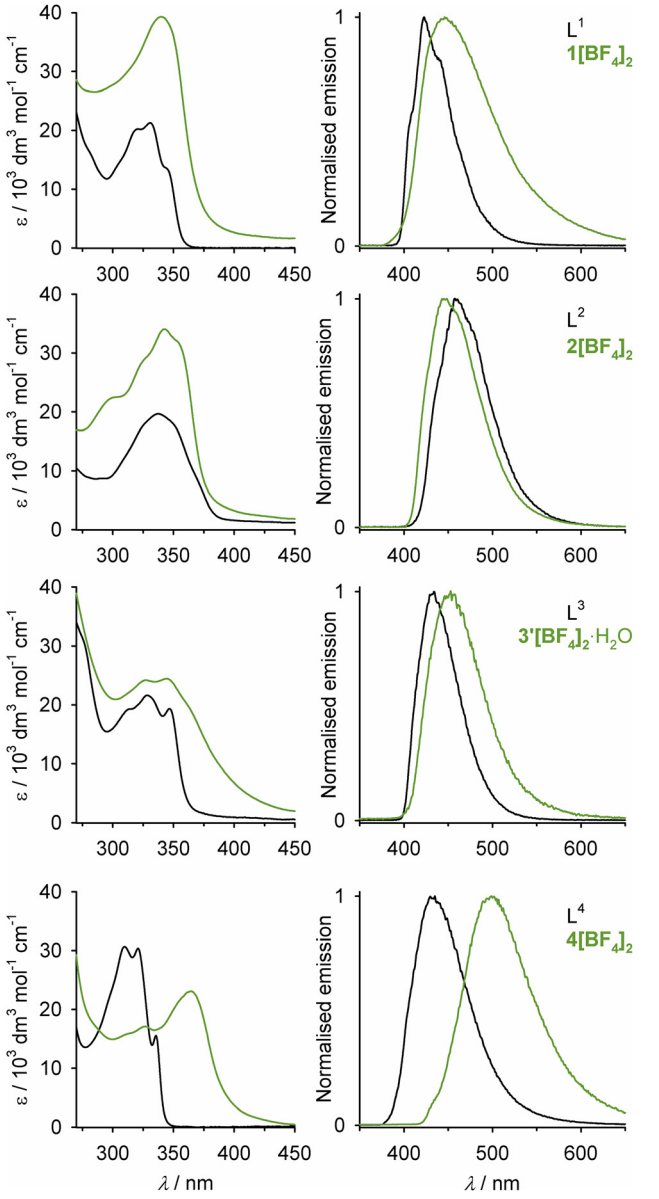

Fig. 7 Absorption spectra (left) and normalised emission spectra (right) from the compounds in this work, in acetonitrile solution at 298 K. The UV-vis extinction coefficients for L^1–L^3 have larger errors, because of their poor solubility. Data from these spectra are listed in Table S10.†

[Fe(L^1)$_2$]$^{2+}$ (**1^{2+}**) and [Fe(L^2)$_2$]$^{2+}$ (**2^{2+}**). The spin states of [Fe(bimpy)$_2$]$^{2+}$ and [Fe(2-bip)$_2$]$^{2+}$, which are isosteric constitutional isomers of **1^{2+}**, were also examined (Table 4). The corresponding metal-free ligands were minimised by the same protocol, in conformations consistent with tridentate coordination to a metal ion.

The computed Fe–N bond lengths lie within 2.4% of the available crystallographic data, in both spin states (Table S12†). That is a reasonable level of agreement for a calculation of this type. While the complexes mostly minimised to geometries with minor deviations from D_{2d} symmetry, [Fe(L^4)$_2$]$^{2+}$ (**4^{2+}**) was computed with a helical conformation that

Table 4 Minimized gas-phase spin state energies for the complexes in this work, and their experimental solution-phase SCO mid-point temperatures ($T_{\frac{1}{2}}$; HS = high-spin). Previously published data for the reference molecule $[Fe(bpp)_2]^{2+}$ computed by the same protocol are also given, for comparison. The lone pair orbital energies used to calculate $E_{av}\{LP\}$ are given in Table S11†

	$T_{\frac{1}{2}}$, K	E(HS), Ha	E(LS), Ha	ΔE\{HS–LS\}, kcal mol^{-1}	ΔE_{rel}\{HS–LS\},[a] kcal mol^{-1}	Free ligand E_{av}\{LP\}, eV
$[Fe(L^1)_2]^{2+}$ ($\mathbf{1}^{2+}$)	237 ± 3	−3273.967089	−3273.987838	+13.0	0	−5.66
$[Fe(L^2)_2]^{2+}$ ($\mathbf{2}^{2+}$)	251 ± 1	−3338.084900	−3338.111325	+16.6	+3.6	−5.73
$[Fe(L^3)_2]^{2+}$ ($\mathbf{3}^{2+}$)	—[b]	−3888.377301	−3888.398581	+13.6	+0.3	−5.69
$[Fe(L^4)_2]^{2+}$ ($\mathbf{4}^{2+}$)	HS	−3362.198522	−3362.213259	+9.3	−3.7	−5.43
$[Fe(bimpy)_2]^{2+}$	331 ± 5[c]	−3274.011814	−3274.038130	+16.8	+3.5	−5.93[d]
$[Fe(2\text{-bip})_2]^{2+}$	212 ± 10[e]	−3273.839226	−3273.859677	+12.8	−0.2	−6.47

[a] A positive ΔE_{rel}\{HS–LS\} means the low-spin state is computed to be more stable than for $\mathbf{1}^{2+}$, and *vice versa*. [b] Not available. [c] In acetone solution.[48,116] [d] From ref. 112. [e] From ref. 66. This value has a larger error because of the limited temperature range of the measurement.

closely resembles its crystal structure (Fig. S47†). Hence, the crystallographic geometry in $\mathbf{4}[\mathbf{BF_4}]_2$ is not a crystal packing artefact, but is an intrinsic property of the molecule. It probably arises from intramolecular steric repulsion involving the quinolyl *C*8–H groups, as discussed above.[93]

As a pure GGA functional, calculations using B86PW91 consistently overstabilise the low-spin states of metal complexes.[113,114] Hence, the spin state energies in Table 4 (ΔE_{rel}\{HS–LS\}) are expressed relative to $\mathbf{1}^{2+}$.[66] A positive ΔE_{rel}\{HS–LS\} means the low-spin state is computed to be more stable than for $\mathbf{1}^{2+}$ implying a higher $T_{\frac{1}{2}}$, and *vice versa*. The ΔE_{rel}\{HS–LS\} values follow the trend:

$$\mathbf{4}^{2+} < [Fe(2\text{-bip})_2]^{2+} < \mathbf{1}^{2+} \approx \mathbf{3}^{2+} < \mathbf{2}^{2+} \approx [Fe(bimpy)_2]^{2+}$$

This agrees with the available experimental data, except that the computed low-spin state of $\mathbf{2}^{2+}$ appears overstabilised compared to the other molecules (Fig. 8). With reference to our previous studies, the positive ΔE_{rel}\{HS–LS\} for $\mathbf{2}^{2+}$ seems *ca.* 5× larger than expected when comparing two compounds whose $T_{\frac{1}{2}}$ values differ by just 14 K.[108–112]

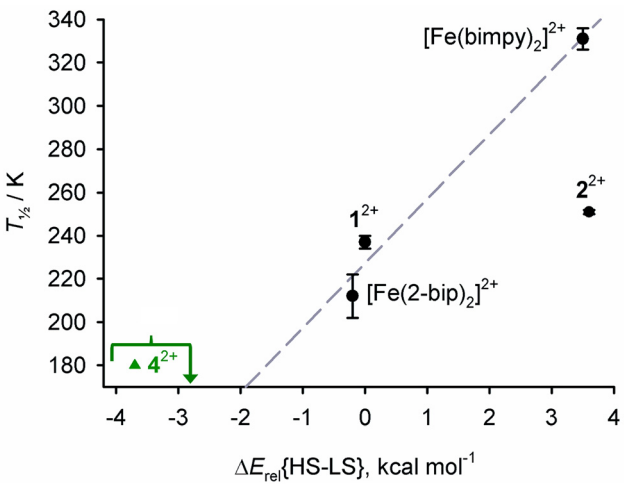

Fig. 8 Correlation between measured solution $T_{\frac{1}{2}}$ values, and the computed spin state energies in Table 4. The line shows the best fit linear regression of the data points for $\mathbf{1}^{2+}$, $[Fe(bimpy)_2]^{2+}$ and $[Fe(2\text{-bip})_2]^{2+}$.[116] Compounds that experimentally show SCO are black circles, and high-spin $\mathbf{4}^{2+}$ ($T_{\frac{1}{2}} \leq 180$ K) is a green triangle.

Gas phase minimisations of sterically crowded molecules using our protocol can overstabilise the high-spin state, with respect to analogous molecules lacking bulky substituents. We attributed this to intramolecular dispersion interactions between atoms from different residues which are in close contact in the molecule.[110,111] Intramolecular dispersion is not included in our protocol, and is difficult to model accurately in single-point DFT calculations.[115] $\mathbf{1}^{2+}$, $\mathbf{3}^{2+}$, $\mathbf{4}^{2+}$, $[Fe(bimpy)_2]^{2+}$ and $[Fe(2\text{-bip})_2]^{2+}$ experience weak inter-ligand C–H···π contacts involving their distal benzo groups but $\mathbf{2}^{2+}$ does not, since the relevant C–H groups are replaced by N atoms in that molecule. Hence, since $\mathbf{2}^{2+}$ should experience less intramolecular dispersion, its ΔE_{rel}\{HS–LS\} may not be strictly comparable with the other molecules in the table.

The ligand Brønsted basicities were compared from the average energies of their three lone pair combination MOs (E_{av}\{LP\}, Table 4). These give the following trend, where the most basic ligand has the highest average lone pair energy:

$$\text{2-bip} < \text{bimpy} < L^2 \approx L^3 \approx L^1 < L^4$$

That is, 2-bip is the least σ-donating ligand in the series and L^4 is the strongest. That ordering does not correlate perfectly with the spin states of their complexes, implying the ligand σ-bonding character is not the sole contributor to their different spin state properties. The high-spin nature of $\mathbf{4}^{2+}$, containing the most σ-basic ligand L^4, reflects the intramolecular steric hindrance in that molecule.[111] The spin states of the other complexes in the study should be less affected by steric factors, however.

Comparison of their frontier orbital energies shows L^2 and 2-bip are the most π-acidic of the remaining ligands, and that $\mathbf{2}^{2+}$ and $[Fe(2\text{-bip})_2]^{2+}$ exhibit greater M–L π-back-bonding than the other complexes in the table. That explains the higher $T_{\frac{1}{2}}$ shown experimentally by $\mathbf{2}[\mathbf{BF_4}]_2$, although this is over-estimated by the calculation. Similarly the stronger π-ligand field in $[Fe(2\text{-bip})_2]^{2+}$ partly offsets its weaker Fe–N σ-bonding, leading to just slightly lower ΔE_{rel}\{HS–LS\} and $T_{\frac{1}{2}}$ values than $\mathbf{1}[\mathbf{BF_4}]_2$.

Table 5 Computed energies for the minimised geometric distortions of high-spin $[Fe(L^1)_2]^{2+}$ and $[Fe(L^2)_2]^{2+}$. ϕ is the *trans*-N{pyridyl}–Fe–N{pyridyl} bond angle[84,85]

	ϕ, deg	E, Ha	ΔE\{dist\},[a] kcal mol^{-1}
$[Fe(L^1)_2]^{2+}$ ($\mathbf{1}^{2+}$)	180	−3273.967089[b]	0
	165[c]	−3273.965652	+0.9
	160[c]	−3273.964194	+1.8
	155[c]	−3273.962500	+2.9
$[Fe(L^2)_2]^{2+}$ ($\mathbf{2}^{2+}$)	180	−3338.084900[b]	0
	165[c]	−3338.083875	+0.6
	160[c]	−3338.083074	+1.2
	155[c]	−3338.081760	+2.0

[a] ΔE(dist) is the energy relative to the corresponding undistorted molecule with ϕ = 180°. [b] Table 4. [c] Fixed during the calculation.

Unlike the other complexes in Fig. 8, the stabilised low-spin state in $[Fe(bimpy)_2]^{2+}$ does not clearly relate to the electronic or steric properties of the bimpy ligand. Thus, no single factor contributing to its larger ΔE_{rel}\{HS–LS\} could be identified from its low-spin d-orbital energies. The π-orbitals of 1*H*-(benz)imidazolyl groups significantly rehybridise upon dative bond formation, which complicates the analysis of the bonding in that complex.[117]

The minimisations of $\mathbf{2}^{2+}$ deviate only slightly from idealised D_{2d} symmetry, which contrasts with the distorted coordination geometry found in crystals of $\mathbf{2}[\mathbf{BF_4}]_2$ (Fig. 2, Table 2). This was investigated by additional minimisations of high-spin $\mathbf{1}^{2+}$ and $\mathbf{2}^{2+}$, with ϕ fixed at values between 165 and 155°.[84] This range of distortions carries an energy penalty of <3 kcal mol^{-1} for $\mathbf{1}^{2+}$, and ≤2 kcal mol^{-1} for $\mathbf{2}^{2+}$ (ΔE\{dist\}, Table 5). Since these values lie above kT (0.6 kcal mol^{-1} at 298 K), the population of distorted molecules in solution should be relatively small at room temperature. We conclude that the distorted geometries observed for $\mathbf{2}[\mathbf{BF_4}]_2$ are probably induced by crystal packing effects.

ΔE\{dist\} for $\mathbf{1}^{2+}$ and $\mathbf{2}^{2+}$ is 2–3× larger than for $[Fe(1\text{-bpp})_2]^{2+}$ (1-bpp = 2,6-di\{pyrazol-1-yl\}pyridine) at each value of ϕ, by the same computational protocol.[108] That indicates the steric influence of the annelated distal ligand donor groups on the distorted coordination geometries of $\mathbf{1}^{2+}$ and $\mathbf{2}^{2+}$.

Conclusions

We have surveyed the iron chemistry of 2,6-bis(imidazo[1,2-*a*]pyridin-2-yl)pyridine (L^1), and two new derivatives L^2 and L^3. While they undergo thermal SCO equilibria in solution, the homoleptic complexes $\mathbf{1}[\mathbf{BF_4}]_2$ and $\mathbf{2}[\mathbf{BF_4}]_2$ mostly form high-spin solvates in the crystalline phase. SCO may be inhibited by an intermolecular contact between complex molecules in the $\mathbf{1}[\mathbf{BF_4}]_2$ solvates (Fig. 1), while $\mathbf{2}[\mathbf{BF_4}]_2$ adopts a distorted coordination geometry in the crystal that favours a high-spin state (Fig. 2). In the latter case, the geometric distortion is coupled to a pattern of intramolecular n···π and intermolecular π···π and C–H···N interactions that is consistently found in all the solvates examined. However, crystalline $\mathbf{1}[\mathbf{BF_4}]_{1.6}[\mathbf{SiF_6}]_{0.2}\cdot 1.7MeNO_2\cdot 0.3Et_2O$ is low-spin at 120 K, confirming that the low-spin state of that complex is thermally accessible.

Unexpectedly the homoleptic iron(II) complex of L^3 was not isolated and is less stable in solution than $\mathbf{1}[\mathbf{BF_4}]_2$ and $\mathbf{2}[\mathbf{BF_4}]_2$ by ^{1}H NMR. A 1 : 1 Fe : L^3 complex was structurally characterised, which shows no unexpected features (Fig. 4).

A crystal structure of a salt of $[Fe(L^4)_2]^{2+}$, $\mathbf{4}[\mathbf{BF_4}]_2$, is also reported. That molecule adopts a strongly flattened six-coordinate geometry with a helical ligand conformation, which is imposed by an inter-ligand steric clash involving its quinolyl *C*8–H groups.[93] The molecular helicity in $\mathbf{4}[\mathbf{BF_4}]_2$ is more pronounced than for the only other structurally characterised $[M(L^4)_2]^{n+}$ complex (M^{n+} = Co^{2+})[93] but was reproduced by a gas phase DFT minimisation, showing it is an intrinsic property of the molecule.

All the complexes in this work are high-spin in solution at room temperature and show a blue ligand-based emission under ambient conditions (Fig. 8). In most cases, this occurs at longer wavelength than the corresponding metal-free ligand emission. An exception is $\mathbf{2}[\mathbf{BF_4}]_2$, whose emission maximum is similar to $\mathbf{1}[\mathbf{BF_4}]_2$ but is slightly blue-shifted compared to L^2. That may reflect the influence of dipolar interactions between the solvent molecules and the L^2 imidazopyrimidinyl *N*8 atoms[93] on that ligand emission.[102] Such interactions should be significant in the free ligand but less so in $\mathbf{2}[\mathbf{BF_4}]_2$, where those N atoms become sterically inaccessible to the environment.

Gas phase DFT calculations mostly reproduce the spin state properties of $\mathbf{1}^{2+}$–$\mathbf{4}^{2+}$, and two constitutional isomers of $\mathbf{1}^{2+}$ from the literature (Table 4). However they overstabilise the low-spin state of $\mathbf{2}^{2+}$ compared to the other molecules, which could reflect weaker intramolecular dispersion interactions in $\mathbf{2}^{2+}$ arising from its reduced steric crowding. The high-spin state and helical molecular geometry of $\mathbf{4}^{2+}$ are reproduced well by the calculation. The ΔE_{rel}\{HS–LS\} spin state energies of the other molecules do not correlate with the ligand σ-basicities, but can be understood as a combination of the metal–ligand σ-bonding and π-bonding character of each ligand.

As well as continuing our synthetic studies, we are seeking a more accurate computational protocol for the spin states of sterically hindered molecules, so the effect of steric crowding in such compounds can be accurately determined. That would have wider value for the design of base metal catalysts for oxidation reactions or other organic transformations, whose mechanisms and effectiveness depend on the spin state of the metal centre.[118,119]

Experimental

Ligands L^1 (ref. 68) and L^4 (Scheme 1)[74] were synthesised by the literature procedures. Other reagents were purchased commercially and used as supplied. Synthetic protocols for the new ligands L^2 and L^3 and characterisation data for all the ligands used are given in the ESI.†

Synthesis of $[Fe(L^1)_2][BF_4]_2$ ($1[BF_4]_2$)

Reaction of $Fe[BF_4]_2{\cdot}6H_2O$ (0.054 g, 0.16 mmol) with L^1 (0.10 g, 0.32 mmol) in nitromethane (10 cm^3) rapidly yielded a dark red solution. This was filtered to remove a small amount of brown precipitate, and the filtrate was concentrated to *ca.* 5 cm^3 volume. Slow diffusion of diethyl ether vapour into the solution yielded a red powder, which was recrystallised from different solvents to afford the solvated crystals described below. Yield 0.065 g, 48%. Found C, 51.3; H, 3.39; N, 15.2%. Calcd for $C_{38}H_{26}B_2F_8FeN_{10}{\cdot}2H_2O$ C, 51.4; H, 3.40; N, 15.8%. ^{1}H NMR (CD_3CN) δ 2.7 (4H), 4.0 (4H), 5.8 (4H), 23.1 (2H), 23.4 (4H), 41.2 (4H), 63.6 (4H).

Synthesis of $[Fe(L^2)_2][BF_4]_2$ ($2[BF_4]_2$)

Method as above, using L^2 (0.10 g, 0.32 mmol). The product was initially obtained as a cherry red powder, which was recrystallised from different solvents as below. Yield 0.060 g, 44%. Found C, 47.3; H, 2.51; N, 22.8%. Calcd for $C_{34}H_{22}B_2F_8FeN_{14}$ C, 47.7; H, 2.59; N, 22.9%. ^{1}H NMR (CD_3CN) δ 4.1 (4H), 9.9 (4H), 15.2 (2H), 25.0 (4H), 36.0 (4H), 53.3 (4H).

Synthesis of $[FeL^3][BF_4]_2{\cdot}H_2O$ ($3'[BF_4]_2{\cdot}H_2O$)

Method as above, using L^3 (0.13 g, 0.32 mmol). Recrystallisation of the product from common organic solvent combinations consistently yielded a brown powder, which analysed as $[FeL^3][BF_4]_2{\cdot}y$(solvent). The sample reported here was recrystallised from undried nitromethane/diethyl ether. Yield 0.060 g, 44%. Found C, 49.9; H, 2.97; N, 10.3%. Calcd for $C_{27}H_{17}B_2F_8FeN_5{\cdot}H_2O$ C, 49.2; H, 2.91; N, 10.6%.

Synthesis of $[FeBr_2(py)_xL^3]{\cdot}yH_2O$ (py = pyridine)

Addition of hydrated $FeBr_2$ (0.054 g, 0.16 mmol) to a solution of L^3 (0.05 g, 0.12 mmol) in 2,2,2-trifluoroethanol (5 cm^3) yielded a cloudy brown solution. The mixture was stored in a freezer for 1 h to coagulate the precipitate, then filtered. Layering the dark brown filtrate with pyridine at room temperature yielded dark brown prisms at the solvent interface. The crystals have the crystallographic formulation $[FeBr(py)_2L^3]Br{\cdot}0.5H_2O$. However, microanalysis was more consistent with the formula $[FeBr(py)L^3]Br{\cdot}2H_2O$, suggesting some of the pyridine content of the crystals may have been exchanged by atmospheric moisture on exposure to air. Yield 0.060 g, 44%. Found C, 51.5; H, 3.19; N, 11.0%. Calcd for $C_{32}H_{22}Br_2FeN_6{\cdot}2H_2O$ C, 51.8; H, 3.53; N, 11.3%.

Synthesis of $[Fe(L^4)_2][BF_4]_2$ ($4[BF_4]_2$)

Method as for $1[BF_4]_2$, using L^4 (0.10 g, 0.32 mmol). The product crystallised as small red platelets, which rapidly collapsed to an amorphous pink powder upon isolation. Yield 0.060 g, 44%. Found C, 60.8; H, 3.47; N, 8.69%. Calcd for $C_{46}H_{30}B_2F_8FeN_6{\cdot}H_2O$ C, 60.4; H, 3.53; N, 9.19%. ^{1}H NMR (CD_3CN) δ −12.1 (2H), 2.5 (4H), 9.0 (4H), 9.5 (4H), 10.5 (4H), 30.3 (4H), 61.8 (4H), 73.6 (4H).

The perchlorate salt of this complex has been reported previously.[73]

Single crystal structure analyses

Solvate crystals of $1[BF_4]_2$, $2[BF_4]_2$ and $4[BF_4]_2$ were grown by slow diffusion of diethyl ether antisolvent vapour, into solutions of each complex in the appropriate solvent. The crystals of $[FeBr(py)_2L^3]Br{\cdot}0.5H_2O$ were obtained from a solvent layering experiment, as described above.

Experimental details and refinement protocols for the structure determinations are given in the ESI.† All the structures were solved by direct methods (SHELX-TL[120]), and developed by full least-squares refinement on F^2 (SHELXL2018[121]). Crystallographic figures were produced using XSEED,[122] and other publication materials were prepared with OLEX2.[123] Unless otherwise stated, the following procedures were applied to the refinements.

Other measurements

Elemental microanalyses were performed by the microanalytical services at the University of Leeds and London Metropolitan University. Diamagnetic NMR spectra employed a Bruker AV3HD spectrometer operating at 400.1 MHz (^{1}H) or 100.6 MHz (^{13}C), while paramagnetic ^{1}H NMR spectra were obtained with a Bruker AV3 spectrometer operating at 300.1 MHz. X-ray powder diffraction data were obtained with a Bruker D8 Advance A25 diffractometer using Cu-K_α radiation (λ = 1.5418 Å).

Solid state magnetic susceptibility measurements were performed on a Quantum Design MPMS-3 magnetometer, with an applied field of 5000 G and a scan rate of 5 K min^{-1}. A diamagnetic correction for the sample was estimated from Pascal's constants;[124] a diamagnetic correction for the sample holder was also applied. Solvated samples were protected against solvent loss by saturating the (tightly sealed) sample holder capsules with a drop of diethyl ether. Magnetic measurements in solution were obtained by Evans method using a JEOL ECA600ii or a Bruker AV500 spectrometer, operating at 600.13 and 500.05 MHz (^{1}H) respectively.[125,126] A diamagnetic correction for the sample,[124] and a correction for the variation of the density of the solvent with temperature,[127] were applied to these data. The parameters in Table 2 were derived by fitting these data to eqn (1) and (2):

$$\ln[(1 - n_{HS}(T))/n_{HS}(T)] = \Delta H/RT - \Delta S/R \quad (1)$$

$$\Delta S = \Delta H/T_{\frac{1}{2}} \quad (2)$$

UV-vis spectra were measured using a PerkinElmer Lambda 900 spectrophotometer. Fluorescence measurements under ambient conditions were obtained using a Horiba Fluoromax 3 fluorimeter with constant slit widths of 2 mm. A range of excitation wavelengths were sampled, and the data quoted are for the excitation wavelength that led to the most intense emission for each compound. The sample concentrations for the fluorescence spectra were between 1–4 × 10^{-5} mol dm^{-3}.

DFT calculations were carried out using SPARTAN'20 for Windows,[128] with the B86PW91 functional and the def2-SVP basis set. Low-spin systems were treated as spin-restricted, and

high-spin systems were treated as spin-unrestricted. The calculations were carried out in the gas phase, since a solvent gradient for iron is not implemented in SPARTAN'20. The molecules were constructed *de novo* in the program, then subjected to a preliminary molecular mechanics minimisation before the full DFT energy minimisation was undertaken.

Data availability

Data supporting this study are available in the ESI,† or at **https://doi.org/10.5518/1413**.

Author contributions

RK did all the experimental work in the publication. MAH conceived and supervised the study, assisted with the crystal structure refinements, performed the DFT calculations and wrote the manuscript draft. Both authors approved the final version of the publication.

Conflicts of interest

There are no conflicts to declare.

Acknowledgements

This work was funded by the EPSRC (EP/K012576/1). The authors thank Simon Barrett (School of Chemistry, University of Leeds) for the Evans method study, and Dr Oscar Cespedes (School of Physics and Astronomy, University of Leeds) for help with the solid state magnetic measurements.

References

1 *Spin Crossover in Transition Metal Compounds I–III: Topics in Current Chemistry*, ed. P. Gütlich and H. A. Goodwin, Springer-Verlag, Berlin, 2004, vol. 233–235.
2 *Spin-crossover materials – properties and applications*, ed. M. A. Halcrow, John Wiley & Sons, Chichester, UK, 2013, p. 568.
3 J. Zarembowitch, F. Varret, A. Hauser, J. A. Real and K. Boukheddaden, *C. R. Chim.*, 2018, **21**, 1056.
4 K. Senthil Kumar, Y. Bayeh, T. Gebretsadik, F. Elemo, M. Gebrezgiabher, M. Thomas and M. Ruben, *Dalton Trans.*, 2019, **48**, 15321.
5 W. Huang, X. Ma, O. Sato and D. Wu, *Chem. Soc. Rev.*, 2021, **50**, 6832.
6 M. Puri and L. Que Jr., *Acc. Chem. Res.*, 2015, **48**, 2443–2452.
7 M. Milan, M. Salamone, M. Costas and M. Bietti, *Acc. Chem. Res.*, 2018, **51**, 1984–1995.
8 M. Guo, T. Corona, K. Ray and W. Nam, *ACS Cent. Sci.*, 2019, **5**, 13–28.
9 P. Chirik and R. Morris, *Acc. Chem. Res.*, 2015, **48**, 2495.
10 M. Beller, *Chem. Rev.*, 2019, **119**, 2089.
11 C. Förster and K. Heinze, *Chem. Soc. Rev.*, 2020, **49**, 1057–1070.
12 C. E. Housecroft and E. C. Constable, *Chem. Sci.*, 2022, **13**, 1225–1262.
13 M. A. Halcrow, *Dalton Trans.*, 2020, **49**, 15560–15567.
14 P. Guionneau, M. Marchivie and G. Chastanet, *Chem. – Eur. J.*, 2021, **27**, 1483–1486.
15 S. Xue, Y. Guo and Y. Garcia, *CrystEngComm*, 2021, **23**, 7899–7915.
16 M. Chergui and E. Collet, *Chem. Rev.*, 2017, **117**, 11025–11065.
17 K. J. Gaffney, *Chem. Sci.*, 2021, **12**, 8010–8025.
18 S. Pillet, *J. Appl. Phys.*, 2021, **129**, 181101.
19 K. Senthil Kumar and M. Ruben, *Angew. Chem., Int. Ed.*, 2021, **60**, 7502–7521.
20 L. Kipgen, M. Bernien, F. Tuczek and W. Kuch, *Adv. Mater.*, 2021, **33**, 2008141 and 2021, **33**, 2170354 [correction].
21 V. Tangoulis, C. D. Polyzou, P. Gkolfi, N. Lalioti, O. Malina and M. Polaskova, *Dalton Trans.*, 2021, **50**, 3109–3115.
22 J. M. Cain, W. He, I. Maurin, M. W. Meisel and D. R. Talham, *J. Appl. Phys.*, 2021, **129**, 160903.
23 G. D. Harzmann, R. Frisenda, H. S. J. van der Zant and M. Mayor, *Angew. Chem., Int. Ed.*, 2015, **54**, 13425–13430.
24 S. K. Karuppannan, A. Martín-Rodríguez, E. Ruiz, P. Harding, D. J. Harding, X. Yu, A. Tadich, B. Cowie, D. Qi and C. A. Nijhuis, *Chem. Sci.*, 2021, **12**, 2381–2388.
25 S. Johannsen, S. Ossinger, J. Grunwald, A. Herman, H. Wende, F. Tuczek, M. Gruber and R. Berndt, *Angew. Chem., Int. Ed.*, 2022, **61**, e202115892.
26 G. Molnár, S. Rat, L. Salmon, W. Nicolazzi and A. Bousseksou, *Adv. Mater.*, 2018, **30**, 1703862.
27 E. Coronado, *Nat. Rev. Mater.*, 2020, **5**, 87–104.
28 O. Kahn, J. Krober and C. Jay, *Adv. Mater.*, 1992, **4**, 718–728.
29 E. Resines-Urien, E. Fernandez-Bartolome, A. Martinez-Martinez, A. Gamonal, L. Piñeiro-López and J. S. Costa, *Chem. Soc. Rev.*, 2023, **52**, 705–727.
30 M. Mikolasek, M. D. Manrique-Juarez, H. J. Shepherd, K. Ridier, S. Rat, V. Shalabaeva, A.-C. Bas, I. E. Collings, F. Mathieu, J. Cacheux, T. Leichle, L. Nicu, W. Nicolazzi, L. Salmon, G. Molnár and A. Bousseksou, *J. Am. Chem. Soc.*, 2018, **140**, 8970–8979.
31 M. D. Manrique-Juárez, F. Mathieu, A. Laborde, S. Rat, V. Shalabaeva, P. Demont, O. Thomas, L. Salmon, T. Leichle, L. Nicu, G. Molnár and A. Bousseksou, *Adv. Funct. Mater.*, 2018, **28**, 1801970.
32 S. P. Vallone, A. N. Tantillo, A. M. dos Santos, J. Molaison, R. Kulmaczewski, A. Chapoy, P. Ahmadi, M. A. Halcrow and K. G. Sandeman, *Adv. Mater.*, 2019, **31**, 1807334.

33 K. Ridier, Y. Zhang, M. Piedrahita-Bello, C. M. Quintero, L. Salmon, G. Molnár, C. Bergaud and A. Bousseksou, *Adv. Mater.*, 2020, **32**, 2000987.
34 M. Romanini, Y. Wang, K. Gürpinar, G. Ornelas, P. Lloveras, Y. Zhang, W. Zheng, M. Barrio, A. Aznar, A. Gràcia-Condal, B. Emre, O. Atakol, C. Popescu, H. Zhang, Y. Long, L. Balicas, J. L. Tamarit, A. Planes, M. Shatruk and L. Mañosa, *Adv. Mater.*, 2021, **33**, 2008076.
35 J. Seo, J. D. Braun, V. M. Dev and J. A. Mason, *J. Am. Chem. Soc.*, 2022, **144**, 6493–6503.
36 M. K. Javed, A. Sulaiman, M. Yamashita and Z.-Y. Li, *Coord. Chem. Rev.*, 2022, **467**, 214625.
37 K. Sun, J.-P. Xue, Z.-S. Yao and J. Tao, *Dalton Trans.*, 2022, **51**, 16044–16054.
38 M. Wang, Z.-Y. Li, R. Ishikawa and M. Yamashita, *Coord. Chem. Rev.*, 2021, **435**, 213819.
39 R. Ababei, C. Pichon, O. Roubeau, Y.-G. Li, N. Bréfuel, L. Buisson, P. Guionneau, C. Mathoniére and R. Clérac, *J. Am. Chem. Soc.*, 2013, **135**, 14840–14853.
40 D. Pinkowicz, M. Rams, M. Mišek, K. V. Kamenev, H. Tomkowiak, A. Katrusiak and B. Sieklucka, *J. Am. Chem. Soc.*, 2015, **137**, 8795–8802.
41 M. Darawsheh, L. A. Barrios, O. Roubeau, S. J. Teat and G. Aromí, *Angew. Chem., Int. Ed.*, 2018, **57**, 13509–13513.
42 Y. Sekine, R. Akiyoshi and S. Hayami, *Coord. Chem. Rev.*, 2022, **469**, 214663.
43 A. Enriquez-Cabrera, A. Rapakousiou, M. Piedrahita Bello, G. Molnár, L. Salmon and A. Bousseksou, *Coord. Chem. Rev.*, 2020, **419**, 213396.
44 H. A. Goodwin, *Top. Curr. Chem.*, 2004, **233**, 59–90.
45 M. A. Halcrow, *Polyhedron*, 2007, **26**, 3523–3576.
46 G. J. Long, F. Grandjean and D. L. Reger, *Top. Curr. Chem.*, 2004, **233**, 91–122.
47 O. G. Shakirova and L. G. Lavrenova, *Crystals*, 2020, **10**, 843.
48 M. Boča, R. F. Jameson and W. Linert, *Coord. Chem. Rev.*, 2011, **255**, 290–317.
49 M. A. Halcrow, *Coord. Chem. Rev.*, 2009, **253**, 2493–2514.
50 J. Olguín and S. Brooker, *Coord. Chem. Rev.*, 2011, **255**, 203–240.
51 L. J. Kershaw Cook, R. Mohammed, G. Sherborne, T. D. Roberts, S. Alvarez and M. A. Halcrow, *Coord. Chem. Rev.*, 2015, **289–290**, 2–12.
52 G. A. Craig, O. Roubeau and G. Aromí, *Coord. Chem. Rev.*, 2014, **269**, 13–31.
53 T. Buchen and P. Gütlich, *Inorg. Chim. Acta*, 1995, **231**, 221–223.
54 J. M. Holland, S. A. Barrett, C. A. Kilner and M. A. Halcrow, *Inorg. Chem. Commun.*, 2002, **5**, 328–332.
55 L. J. Kershaw Cook, R. Kulmaczewski, R. Mohammed, S. Dudley, S. A. Barrett, M. A. Little, R. J. Deeth and M. A. Halcrow, *Angew. Chem., Int. Ed.*, 2016, **55**, 4327–4331.
56 I. Nikovskiy, A. Polezhaev, V. Novikov, D. Aleshin, A. Pavlov, E. Saffiulina, R. Aysin, P. Dorovatovskii, L. Nodaraki, F. Tuna and Y. Nelyubina, *Chem. – Eur. J.*, 2020, **26**, 5629–5638.
57 R. Akiyoshi, Y. Hirota, D. Kosumi, M. Tsutsumi, M. Nakamura, L. F. Lindoy and S. Hayami, *Chem. Sci.*, 2019, **10**, 5843–5848.
58 Ö. Üngör, E. S. Choi and M. Shatruk, *Chem. Sci.*, 2021, **12**, 10765–10779.
59 E. J. Devid, P. N. Martinho, M. V. Kamalakar, I. Šalitroš, U. Prendergast, J.-F. Dayen, V. Meded, T. Lemma, R. González-Prieto, F. Evers, T. E. Keyes, M. Ruben, B. Doudin and S. J. van der Molen, *ACS Nano*, 2015, **9**, 4496–4507.
60 A. Abhervé, M. Palacios-Corella, J. M. Clemente-Juan, R. Marx, P. Neugebauer, J. van Slageren, M. Clemente-León and E. Coronado, *J. Mater. Chem. C*, 2015, **3**, 7936–7945.
61 B. Schäfer, T. Bauer, I. Faus, J. A. Wolny, F. Dahms, O. Fuhr, S. Lebedkin, H.-C. Wille, K. Schlage, K. Chevalier, F. Rupp, R. Diller, V. Schünemann, M. M. Kappes and M. Ruben, *Dalton Trans.*, 2017, **46**, 2289–2302.
62 I. Šalitroš, R. Herchel, O. Fuhr, R. González-Prieto and M. Ruben, *Inorg. Chem.*, 2019, **58**, 4310–4319.
63 M. Palacios-Corella, J. Ramos-Soriano, M. Souto, D. Ananias, J. Calbo, E. Ortí, B. M. Illescas, M. Clemente-León, N. Martín and E. Coronado, *Chem. Sci.*, 2021, **12**, 757–766.
64 I. Galadzhun, R. Kulmaczewski, N. Shahid, O. Cespedes, M. J. Howard and M. A. Halcrow, *Chem. Commun.*, 2021, **57**, 4039–4042.
65 M. Hasegawa, F. Renz, T. Hara, Y. Kikuchia, Y. Fukuda, J. Okubo, T. Hoshi and W. Linert, *Chem. Phys.*, 2002, **277**, 21–30.
66 A. Santoro, L. J. Kershaw Cook, R. Kulmaczewski, S. A. Barrett, O. Cespedes and M. A. Halcrow, *Inorg. Chem.*, 2015, **54**, 682–693.
67 S. Vela, C. Gourlaouen, M. Fumanal and J. Ribas-Arino, *Magnetochemistry*, 2016, **2**, 6.
68 K. Li, J.-L. Niu, M.-Z. Yang, Z. Li, L.-Y. Wu, X.-Q. Hao and M.-P. Song, *Organometallics*, 2015, **34**, 1170–1176.
69 F.-L. Yang, X. Zhu, D.-K. Rao, X.-N. Cao, K. Li, Y. Xu, X.-Q. Hao and M.-P. Song, *RSC Adv.*, 2016, **6**, 37093–37098.
70 F.-L. Yang, Y.-H. Wang, Y.-F. Ni, X. Gao, B. Song, X. Zhu and X.-Q. Hao, *Eur. J. Org. Chem.*, 2017, 3481–3486.
71 X.-N. Cao, X.-M. Wan, F.-L. Yang, K. Li, X.-Q. Hao, T. Shao, X. Zhu and M.-P. Song, *J. Org. Chem.*, 2018, **83**, 3657–3668.
72 X.-M. Wan, Z.-L. Liu, W.-Q. Liu, X.-N. Cao, X. Zhu, X.-M. Zhao, B. Song, X.-Q. Hao and G. Liu, *Tetrahedron*, 2019, **75**, 2697–2705.
73 C. M. Harris, H. R. H. Patil and E. Sinn, *Inorg. Chem.*, 1969, **8**, 101–104.
74 E. Largy, F. Hamon, F. Rosu, V. Gabelica, E. De Pauw, A. Guédin, J.-L. Mergny and M.-P. Teulade-Fichou, *Chem. – Eur. J.*, 2011, **17**, 13274–13283.

75 M. Hostettler, K. W. Törnroos, D. Chernyshov, B. Vangdal and H.-B. Bürgi, *Angew. Chem., Int. Ed.*, 2004, **43**, 4589–4594.
76 I. Nemec, R. Herchel and Z. Trávníček, *Dalton Trans.*, 2015, **44**, 4474–4484.
77 L. J. Kershaw Cook, R. Kulmaczewski, O. Cespedes and M. A. Halcrow, *Chem. – Eur. J.*, 2016, **22**, 1789–1799.
78 W. Phonsri, P. Harding, L. Liu, S. G. Telfer, K. S. Murray, B. Moubaraki, T. M. Ross, G. N. L. Jameson and D. J. Harding, *Chem. Sci.*, 2017, **8**, 3949–3959.
79 X.-P. Sun, R.-J. Wei, Z.-S. Yao and J. Tao, *Cryst. Growth Des.*, 2018, **18**, 6853–6862.
80 I. Capel Berdiell, R. Kulmaczewski, N. Shahid, O. Cespedes and M. A. Halcrow, *Chem. Commun.*, 2021, **57**, 6566–6569.
81 L. T. Birchall, A. T. Raja, L. Jackson and H. J. Shepherd, *Cryst. Growth Des.*, 2023, **23**, 1768–1774.
82 V_{Oh} is the volume of the octahedron defined by the FeN_6 coordination sphere.[83] Σ is a general measure of the deviation of a metal ion from an ideal octahedral geometry, while Θ more specifically indicates its distortion towards a trigonal prismatic structure. Σ and Θ are usually larger in the high-spin than in the low-spin state, especially for complexes of chelating ligands with restricted bite angles like L^1 and L^2; a perfectly octahedral complex gives $\Sigma = \Theta = 0$.[83] Full definitions of Σ and Θ are in the ESI.†
83 P. Guionneau, M. Marchivie, G. Bravic, J.-F. Létard and D. Chasseau, *Top. Curr. Chem.*, 2004, **234**, 97–128.
84 θ is the dihedral angle between the least squares planes of the two L ligands, and ϕ is the *trans*-N{pyridyl}–Fe–N{pyridyl} bond angle.[85] An ideal D_{2d}-symmetric geometry for a $[FeL_2]^{2+}$ centre (L = a meridional tridentate ligand) gives $\theta = 90$ and $\phi = 180°$, but many high-spin complexes of this type exhibit significantly reduced values for these parameters. See the ESI† for more details.
85 J. M. Holland, J. A. McAllister, C. A. Kilner, M. Thornton-Pett, A. J. Bridgeman and M. A. Halcrow, *J. Chem. Soc., Dalton Trans.*, 2002, 548–554.
86 P. J. van Koningsbruggen, J. G. Haasnoot, R. A. G. de Graaff and J. Reedijk, *J. Chem. Soc., Dalton Trans.*, 1993, 483–484.
87 I. Dance and M. Scudder, *CrystEngComm*, 2009, **11**, 2233–2247.
88 R. Pritchard, C. A. Kilner and M. A. Halcrow, *Chem. Commun.*, 2007, 577–579.
89 E. Michaels, C. M. Pask, I. Capel Berdiell, H. B. Vasili, M. J. Howard, O. Cespedes and M. A. Halcrow, *Cryst. Growth Des.*, 2022, **22**, 6809–6817.
90 S. Vela, J. J. Novoa and J. Ribas-Arino, *Phys. Chem. Chem. Phys.*, 2014, **16**, 27012–27024.
91 L. J. Kershaw Cook, F. L. Thorp-Greenwood, T. P. Comyn, O. Cespedes, G. Chastanet and M. A. Halcrow, *Inorg. Chem.*, 2015, **54**, 6319–6330.
92 R. Kulmaczewski, I. T. Armstrong, P. Catchpole, E. S. J. Ratcliffe, H. B. Vasili, S. L. Warriner, O. Cespedes and M. A. Halcrow, *Chem. – Eur. J.*, 2023, **29**, e202202578.
93 This atom label corresponds to the IUPAC atom numbering for imidazo[1,2-*a*]pyridyl residues, ed. J. Rigaudy and S. P. Klesney, *Nomenclature of Organic Chemistry, Sections A, B, C, D, E, F, and H*, Pergamon Press, Oxford, 1979, sect. B3.
94 S. Aroua, T. K. Todorova, P. Hommes, L.-M. Chamoreau, H.-U. Reissig, V. Mougel and M. Fontecave, *Inorg. Chem.*, 2017, **56**, 5930–5940.
95 H. Toftlund, *Monatsh. Chem.*, 2001, **132**, 1269–1277.
96 K. P. Kepp, *Inorg. Chem.*, 2016, **55**, 2717–2727.
97 N. Hassan, A. B. Koudriavtsev and W. Linert, *Pure Appl. Chem.*, 2008, **80**, 1281–1292.
98 S. Sundaresan and S. Brooker, *Inorg. Chem.*, 2023, **62**, 12192–12202.
99 J. Catalan, E. Mena, F. Fabero and F. Amat-Guerri, *J. Chem. Phys.*, 1992, **96**, 2005–2016.
100 H. Tomoda, T. Hirano, S. Saito, T. Mutai and K. Araki, *Bull. Chem. Soc. Jpn.*, 1999, **72**, 1327–1334.
101 A. J. Stasyuk, M. Banasiewicz, M. K. Cyrański and D. T. Gryko, *J. Org. Chem.*, 2012, **77**, 5552–5558.
102 D. A. Lerner, P. M. Horowitz and E. M. Evleth, The absorption and emission spectra of imidazo[1,2-a]pyrimidine are solvent-dependent, *J. Phys. Chem.*, 1977, **81**, 12–17.
103 D. M. Klassen, C. W. Hudson and E. L. Shaddix, *Inorg. Chem.*, 1975, **14**, 2733–2736.
104 M. L. Stone and G. A. Crosby, *Chem. Phys. Lett.*, 1981, **79**, 169–173.
105 B. J. Houghton and R. J. Deeth, *Eur. J. Inorg. Chem.*, 2014, 4573–4580.
106 S. R. Mortensen and K. P. Kepp, *J. Phys. Chem. A*, 2015, **119**, 4041–4050.
107 O. S. Siig and K. P. Kepp, *J. Phys. Chem. A*, 2018, **122**, 4208–4217.
108 I. Capel Berdiell, R. Kulmaczewski and M. A. Halcrow, *Inorg. Chem.*, 2017, **56**, 8817–8828.
109 R. Kulmaczewski, M. J. Howard and M. A. Halcrow, *Dalton Trans.*, 2021, **50**, 3464–3467.
110 I. Capel Berdiell, D. J. Davies, J. Woodworth, R. Kulmaczewski, O. Cespedes and M. A. Halcrow, *Inorg. Chem.*, 2021, **60**, 14988–15000.
111 N. Shahid, K. E. Burrows, C. M. Pask, O. Cespedes, M. J. Howard, P. C. McGowan and M. A. Halcrow, *Inorg. Chem.*, 2021, **60**, 14336–14348.
112 N. Shahid, K. E. Burrows, C. M. Pask, O. Cespedes, M. J. Howard, P. C. McGowan and M. A. Halcrow, *Dalton Trans.*, 2022, **51**, 4262–4274.
113 M. Reiher, O. Salomon and B. A. Hess, *Theor. Chem. Acc.*, 2001, **107**, 48–55.
114 S. Zein, S. A. Borshch, P. Fleurat-Lessard, M. E. Casida and H. Chermette, *J. Chem. Phys.*, 2007, **126**, 014105.
115 D. C. Ashley and E. Jakubikova, *Coord. Chem. Rev.*, 2017, **337**, 97–111.
116 $T_{\frac{1}{2}}$ for $[Fe(bimpy)_2]^{2+}$ in solution is solvent-dependent, which reflects the influence of hydrogen bonding between its peripheral N–H groups and the solvent on the metal ion ligand field. It shows $T_{\frac{1}{2}} = 330$–335 K in weakly inter-

acting solvents, which should approximate its environment in the gas phase (ref. 48).
117 Ł. Boda, M. Boczar, M. J. Wójcik and T. Nakajima, *J. Phys. Chem. A*, 2021, **125**, 6902–6912.
118 A. Fürstner, *ACS Cent. Sci.*, 2016, **2**, 778–789.
119 M. Guo, T. Corona, K. Ray and W. Nam, *ACS Cent. Sci.*, 2019, **5**, 13–28.
120 G. M. Sheldrick, *Acta Crystallogr., Sect. A: Found. Adv.*, 2015, **71**, 3–8.
121 G. M. Sheldrick, *Acta Crystallogr., Sect. C: Struct. Chem.*, 2015, **71**, 3–8.
122 L. J. Barbour, *J. Appl. Crystallogr.*, 2020, **53**, 1141–1146.
123 O. V. Dolomanov, L. J. Bourhis, R. J. Gildea, J. A. K. Howard and H. Puschmann, *J. Appl. Crystallogr.*, 2009, **42**, 339–341.
124 C. J. O'Connor, *Prog. Inorg. Chem.*, 1982, **29**, 203–283.
125 D. F. Evans, *J. Chem. Soc.*, 1959, 2003–2005.
126 E. M. Schubert, *J. Chem. Educ.*, 1992, **69**, 62.
127 B. García and J. C. Ortega, *J. Chem. Eng. Data*, 1988, **33**, 200–204.
128 *Spartan'20*, Wavefunction Inc., Irvine CA, USA, 2020.